hydrology

MDPI

Article

Spatiotemporal Patterns of Inundation in the Nemunas River Delta Using Sentinel-1 SAR: Influence of Land Use and Soil Composition

Jonas Gintauskas *, Martynas Bučas, Diana Vaičiūtė and Edvinas Tiškus

Marine Research Institute, Klaipeda University, 92294 Klaipeda, Lithuania; martynas.bucas@ku.lt (M.B.); diana.vaiciute@ku.lt (D.V.); edvinas.tiskus@ku.lt (E.T.)

* Correspondence: jonas.gintauskas@ku.lt

Abstract

Inundation dynamics in low-lying deltas are becoming increasingly important to monitor due to the impacts of climate change and human alterations to hydrological systems, which disrupt natural inundation patterns. In the Nemunas River Delta, where seasonal and extreme floods impact agricultural and natural landscapes, we used Sentinel-1 synthetic aperture radar (SAR) imagery (2015–2019), validated with drone data, to map flood extents. SAR provides consistent, 10 m resolution data unaffected by cloud cover, while drone imagery provides high-resolution (10 cm) data at 90 m flight height for validation during SAR acquisitions. Results revealed peak inundation during spring snowmelt and colder months, with shorter, rainfall-driven summer floods. Approximately 60% of inundated areas were low-lying agricultural fields, which experienced prolonged waterlogging due to poor drainage and soil degradation. Inundation duration was shaped by lithology, land cover, and topography. A consistent 5–10-day lag between peak river discharge and flood expansion suggests discharge data can complement SAR when imagery is unavailable. This study confirms SAR's value for flood mapping in cloud-prone, temperate regions and highlights its scalability for monitoring flood-prone deltas where agriculture and infrastructure face increasing climate-related risks.

Keywords: flood; inundation; remote sensing; SAR; Nemunas Delta; drone

Academic Editor: Fabio Castelli

Received: 30 July 2025
Revised: 15 September 2025
Accepted: 18 September 2025
Published: 23 September 2025

Citation: Gintauskas, J.; Bučas, M.; Vaičiūtė, D.; Tiškus, E. Spatiotemporal Patterns of Inundation in the Nemunas River Delta Using Sentinel-1 SAR: Influence of Land Use and Soil Composition. *Hydrology* **2025**, *12*, 245. https://doi.org/10.3390/hydrology12100245

1. Introduction

River deltas are highly susceptible to flooding due to their naturally low-lying topography. Additionally, many delta regions support agricultural activities, economically and strategically significant infrastructure, increasing both exposure to flood risks and the potential for damage [1]. Despite existing flood mitigation measures, climate change is exacerbating the vulnerability of river deltas to flooding by changing precipitation patterns and disrupting the natural timing and flow of rivers. More intense and erratic rainfall events are increasing the frequency and severity of floods in these regions [2,3]. A significant consequence is the shifting hydrological year, the period marking the annual cycle of water availability, which can create discrepancies between water supply and seasonal needs for agriculture, ecosystems, and infrastructure [4–7]. These changes intensify existing pressures on river deltas, elevating flood risks and endangering local livelihoods and development.

Tracking yearly patterns of inundations requires innovative research tools, such as remote sensing data. Several studies have utilized optical satellites for flood

monitoring [8–11]. However, the effectiveness of optical satellite imagery is often compromised by cloud cover, which is prevalent in the Baltic region, particularly during the winter and spring months when the most significant flooding events occur [12]. Since cloud cover obstructs the satellite's view of the Earth's surface, it renders the data incomplete or unusable, making consistent and repeatable monitoring difficult [13]. This limitation is especially problematic in areas with frequent cloud cover during critical flooding periods, as it can hinder timely and accurate flood assessment and response. To address this issue, alternative remote sensing technologies, such as Synthetic Aperture Radar (SAR) satellites, are often employed [14–16]. Unlike optical satellites, SAR provides reliable data regardless of cloud cover, weather conditions, or the time of day. This capability makes radar an invaluable tool for continuous and effective flood and inundation monitoring in temperate climate regions, ensuring that critical information is available even during periods of heavy cloud cover.

Various methods are employed to identify inundated areas using SAR data, including change detection techniques that compare pre- and post-event images [17,18], unsupervised classification methods like thresholding and clustering [19–21], and supervised machine learning approaches that rely on labeled training data [22]. The change detection method, which compares data from dry and wet (inundated) periods to map inundation events, is cost-effective and does not require the extensive training phase associated with supervised image classification methods. This efficiency makes the change detection method a practical choice for flood and inundation mapping, especially in areas where on-the-ground data collection may be challenging or expensive. In this study, the implementation of these methods was facilitated by the Google Earth Engine platform, which provides access to large-scale SAR archives and enables automated processing for consistent and reproducible results.

This study addresses two interconnected gaps in the remote sensing of deltaic inundation. First, while SAR is a proven tool for flood detection, its application has been largely limited to short-term or single-event analyses [23,24], with few studies spanning multiple years to capture complete hydrological cycles [25,26]. Second, this lack of long-term data is particularly critical in the most understudied deltaic environments. Whereas considerable research has targeted deltas discharging into open marine systems [27–30], there is an absence of SAR-based flood mapping in deltas terminating in relatively closed deltas, such as the lagoons in the Baltic Sea. The hydrodynamics of these lagoon deltas, dominated by fluvial input rather than tides and are more likely to produce inundation patterns that are more prolonged and spatially complex, making them especially dependent on long-term observation for accurate characterization [31]. Therefore, this research fills a critical need by applying a multi-year SAR change detection methodology to quantify the spatial-temporal inundation dynamics of a lagoon-connected delta.

In this study, we advance the SAR-based change detection approach by incorporating a statistically validated threshold selection process, supported by drone-based validation data. This methodological refinement enhances the robustness and reproducibility of flood mapping, since, to our knowledge, few studies have systematically tested multiple thresholds for flood delineation. Instead, many rely on heuristically derived or semi-automatic thresholds without rigorous validation. Researchers employed semi-automatic thresholding based on manually selected land and water samples [32], acknowledging the challenges of thresholding in large-scale SAR flood mapping but did not validate their chosen thresholds against independent datasets [33]. Some studies highlighted that quantitative validation remains underdeveloped in SAR flood detection research [15]. By contrast, our study introduces a statistically grounded threshold evaluation, contributing to more reliable and transferable flood mapping practices.

The Nemunas River Delta is one of the largest Baltic Sea deltas, known for its intricate network of waterways, numerous islands, and vast floodplains; the delta is particularly prone to seasonal flooding [34], which occurs in the spring, driven by snowmelt from the river's upper basin and increased rainfall [35]. The delta area employs various flood management strategies, such as dikes, polders, and drainage systems, to protect agricultural lands and settlements while maintaining the natural flooding cycle to preserve the delta's ecological balance. Although the climate-driven shift in the hydrological regime is evident in the timing of spring floods, in the type of winter precipitation [36], and in the increase in precipitation and air temperature throughout the year [37–39]. Although there are existing datasets of flooded areas and prepared models for the Nemunas Delta, a significant gap remains due to the absence of real delta-scale data on inundated areas, collected across several years and seasons, which offers greater accuracy than model-based estimations.

Therefore, this study aims to map flooded and inundated areas in the Nemunas Delta using Sentinel-1 SAR imagery from 2015 to 2019. This period was selected due to its hydrological diversity, including two major flooding events in 2017 that produced the maximum observed inundation extent, alongside years with typical seasonal flooding patterns, and the availability of Sentinel-1 data, as no systematic SAR coverage of the region existed prior to its launch in 2014. Thereby, tracking floods and inundation patterns and water expansion, and gaining valuable insights into the evolving dynamics of water inundation in this region. Additionally, we analyzed the inundation pattern using water level measurement stations to determine whether with water discharge data alone we could predict the areas likely to be affected by inundation. We also examined flood patterns in relation to topography, lithology, drainage network density, precipitation, and land use to better understand the physical and anthropogenic factors influencing inundation extent and frequency. Such inundation data is crucial for planning and developing infrastructure in these types of areas, as it allows planners to account for inundation frequency and distribution when designing land use and infrastructure.

2. Materials and Methods

2.1. Study Area

The Nemunas Delta spans the western part of Lithuania and the Russian Kaliningrad territory, where the Nemunas River flows into the Curonian Lagoon before reaching the Baltic Sea. This study focuses on the right bank of the Nemunas Delta (Lithuanian side), where flooding is most frequent, as data limitations restrict analysis of the Russian segment. The delta boundaries were selected based on the delineation by [34], where the area is 515 km^2 (Figure 1).

The floodwaters in Nemunas Delta usually start to rise in March or April, depending on weather conditions. The initial rise in river discharge can result in gradual flooding that persists for several days to a week. The most extensive flooding generally happens about 1–2 weeks after the initial rise, once the upstream snowmelt fully impacts the delta [40].

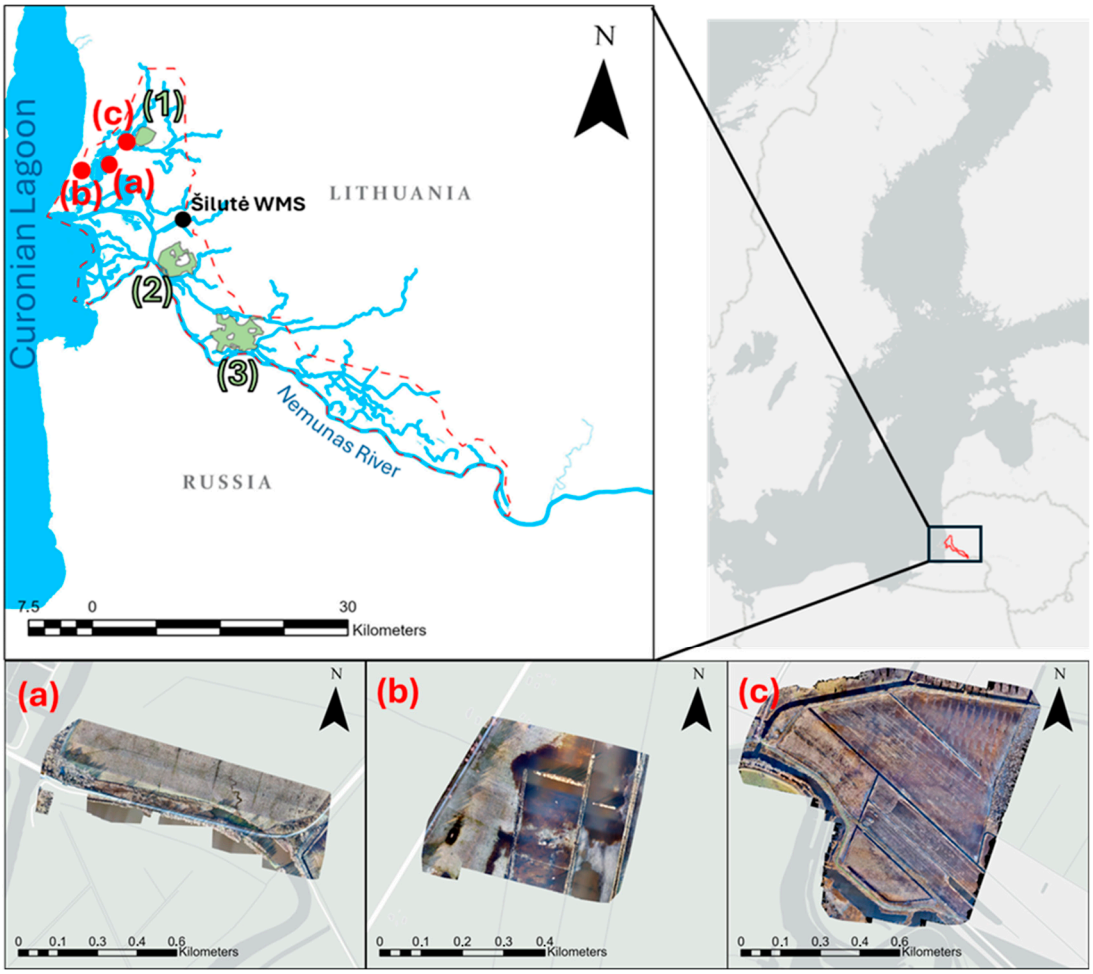

Figure 1. Nemunas Delta part of Lithuania [34] (red dashed line) with Šilutė water measuring station (WMS) location and validation areas mapped by using a drone (**a**) near Kintai town, (**b**) near Muižė village, and (**c**) near Sakūčiai forest. The figure also shows forests adjacent to flood-prone areas: (1) Sakūčiai forest, (2) Žalgiriai forest, and (3) Leitgiriai forest.

2.2. Drone Flights

For the inundated areas classification from SAR data accuracy assessment and validation, we opted to use drone imagery due to its ability to cover larger and more diverse areas than traditional in situ measurements, which are often limited in scope and accessibility [19,41,42]. Drone surveys proved especially useful in the Nemunas Delta, where waterlogged terrain hindered ground access, enabling inundation validation in remote areas. However, unlike SAR, drones lacked consistent wide-area coverage and repeatability. The drones captured 8 cm resolution images from 90 m, enabling detailed assessment of various conditions: open water, complete submergence, partially inundated regions with emergent vegetation, and dry land. These observations were categorized into feature classes and compared with Sentinel-1 satellite data, with drone flights synchronized to the satellite's acquisition time for temporal consistency. The validation was conducted in three areas of the Nemunas Delta, situated at a greater distance from the Russian–Lithuanian border to avoid restrictions and mitigate potential risks associated with flight safety in the border zone. The total validation area covered 1.49 km^2; the first area (0.58 km^2) was surveyed twice on 9 January 2020 and 1 March 2022; the second (0.18 km^2) was surveyed on 1 March 2022; and the third (0.73 km^2) was surveyed on 29 December 2020.

Drone flights were conducted using a DJI Inspire 2 (DJI, Shenzhen, China) equipped with a Zenmuse X5S camera (DJI, Shenzhen, China). The flights were carried out at an

altitude of 90 m, during which each flight mission captured between 500 and 1500 high-resolution photographs. These images were then processed and stitched together into a mosaic using Pix4DMapper v4.7.5 software. This approach allowed for comprehensive aerial coverage of the target area, enabling detailed analysis and mapping with high precision. By comparing the high-resolution images captured by the drone with the satellite data, the accuracy and reliability of the satellite observations could be assessed. Each image was classified manually into water and land categories, and the differences between the classifications were used to generate a confusion matrix (Figure 2).

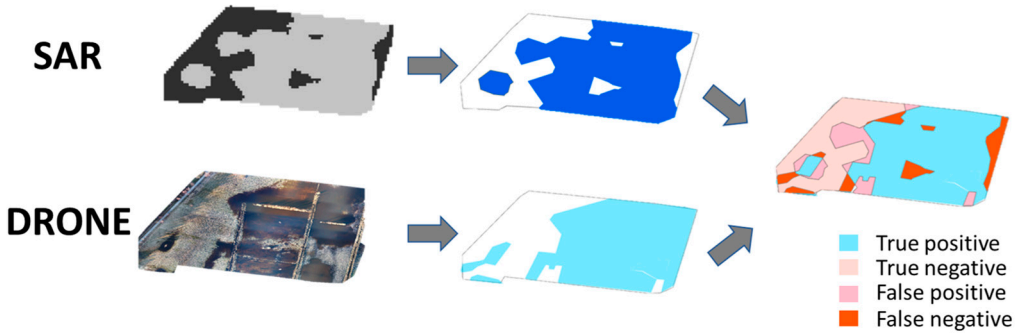

Figure 2. Validation process using SAR imagery (top) and drone imagery (bottom). Dark blue and light blue denote water areas identified after analysis. The final panel shows the combined confusion matrix map integrating both datasets.

2.3. Hydrological Data

The river water measurement station was selected to be located on the edge of the Nemunas Delta plain (Figure 1). At this station, both water discharge and water levels are recorded electronically once per day to monitor hydrological conditions. Its proximity to the Šilutė weather measurement station enables the integration of hydrological data with meteorological observations, particularly precipitation metrics such as snowfall and rainfall.

2.4. Image Processing and Inundation Detection

Google Earth Engine pre-processed data was used for inundation delineation [43]. Specifically, we employed a dataset consisting of 660 Sentinel-1 Ground Range Detected High Resolution (GRDH) Interferometric Wide (IW) images (Table 1). The images were categorized into 220 time periods, throughout the 2015–2019 period, of which 173 were analyzed in detail. Since these periods depend on Sentinel-1 acquisition frequency, they vary in duration rather than following a fixed interval. This selection was necessary because not all satellite orbits fully covered the entire study area, requiring multiple acquisitions to be averaged. The temporal intervals between images varied from 3 to 7 days, which was due to the inconsistent acquisition frequency of Sentinel-1 prior to the operational deployment of Sentinel-1B. This variability in acquisition was particularly noticeable before Sentinel-1B became fully operational in April 2016, which led to gaps in image availability. These time periods were selected to ensure complete coverage of the Nemunas Delta study area, as individual satellite orbits did not always cover the entire region.

A total of 47 time periods were excluded from the analysis due to unfavorable conditions for data collection. These periods were primarily affected by snow cover, which hid the underlying terrain and prevented accurate observation or analysis of the inundated areas beneath. The images were produced through visual inspection after image classification, during which unusual patterns were identified and cross-checked with hydrometeorological data from the Lithuanian Hydrometeorological Agency to confirm the presence of snow during the image acquisition period. The presence of snow significantly

hindered the ability to detect inundation-related changes in the landscape, as the radar signals from Sentinel-1 could not penetrate the snow layer to reveal the ground conditions. Consequently, these periods were deemed unsuitable for reliable inundation delineation and were omitted from further study.

Table 1. Characteristics of the used Sentinel-1 data.

Characteristics of the Used Sentinel-1 Data	
Wavelength	5.6 cm
Mode	IW
Polarization	VV, VH
Frequency	C-Band (GHz)
Resolution	20 × 22 m (ground range and azimuth)
Pixel resolution	10 × 10 m
Incidence angle	29–46°
Product level	Level-1 GRDH
Pass direction	Descending, Ascending
Relative orbit	29 and 51

Change detection techniques were applied by comparing satellite imagery from the driest period of each year against imagery from other seasons. The driest period was determined using hydrometeorological data, specifically the period of lowest rainfall and minimal water levels, which typically occurred in August during the summer season when no rain-induced flooding was present. This approach was adopted to ensure that the data remained significantly unaffected by any permanent changes to the land cover, such as forest management. The analysis focused on variations in the VH (vertical-horizontal) polarization band between the dry and wet periods. If the observed changes in the VH band during the wet period were found to be 1.25 times greater than those in the dry period, this was interpreted as an indication of potential inundation [44].

The regions located beneath the forest canopy, which are not detectable through SAR imagery due to signal attenuation caused by dense vegetation, were supplemented with data derived from Digital Elevation Models (DEM) provided by Lithuanian geographic services. Since SAR is limited in detecting surface conditions under forest cover, the DEM data were used to detect flood presence within these areas by analyzing elevation patterns in the surrounding terrain. If adjacent non-forested areas at a certain elevation were identified as flooded, it was assumed that forested regions at the same elevation were similarly affected. To achieve this, the ArcGIS software [45] was utilized, enabling the integration of these DEM datasets to accurately fill in the gaps created by SAR's limitations in forested areas. This approach ensured comprehensive coverage of the terrain by combining multiple data sources for enhanced precision in areas obstructed by dense vegetation.

2.5. The Relationship Between Inundation Dynamics, Water Discharge, Land Cover, Lithological and Topographic Factors

The study examined the correlation between the initial rise in water discharge recorded at a water monitoring station and the inundation extent observed in SAR classified images. This analysis was conducted with different time delays: no delay, as well as 5-, 10-, and 15-day delays, to account for lag in water spread and detection. This approach was chosen by the variable revisit frequency of Sentinel-1 imagery in the Nemunas Delta, which ranged from 5 to 12 days before the deployment of Sentinel-1B (launched on 25 April 2016), and improved to 2–7 days afterward. The lag analysis aimed to identify the optimal temporal offset between discharge events and SAR-based inundation classification. Furthermore, the

cumulative water discharge over 10 and 15 days was evaluated to determine whether the accumulated water volume could better explain the extent of inundation.

To better understand the relationship between environmental characteristics and inundation dynamics in the Nemunas Delta, geospatial data on lithology, land cover, topography, and hydrology were incorporated into the analysis. A Digital Elevation Model (DEM) was used to calculate elevation and derive terrain characteristics, while a drainage network density layer was developed to quantify the influence of fluvial flow on floodwater distribution. In the Nemunas Delta region, 19 distinct types of lithology were identified: silt, silty clay, silty sand, ombrotrophic peat, peat, peaty sand, various types of loamy sand and sandy loam, different grades of sand, clay, clay loam, sandy loam, sapropel, sandy silt, very fine to fine sand, sand mixed with gravel, fine sand, very fine sand, medium sand, fen peat, and certain unrecognized items [46]. Lithological characteristics were classified into four granulometric classes based on particle size: (1) peat, (2) clay, (3) sand, and (4) coarse sand. These classes, ordered from the finest to the coarsest particles, served as an ordinal variable representing soil texture and its influence on infiltration and drainage. Land cover data were obtained from the 2018 Corine Land Cover dataset, provided by the Copernicus Land Monitoring Service [47]. For the analysis, land cover types were aggregated into broader categories: natural surfaces were derived by combining all forest, semi-natural areas, and wetlands; agricultural areas were retained as is, while artificial surfaces and water bodies were omitted from further consideration.

2.6. Numerical and Spatial Statistical Analysis

The accuracy of inundation classification, validated using drone imagery, was evaluated using the F1 score statistical metric. This metric was derived from a confusion matrix.

The Pearson correlation coefficient was used to evaluate the relationship between river discharge and inundation area under different temporal conditions, such as lag and accumulation [48].

Wilcoxon rank-sum tests [49] were used to assess pairwise differences in inundated area (km^2) across years, using the stats R v4.5.0 package for pairwise comparisons [50].

The relationship between inundation dynamics and land cover, lithological, and topographic factors was modeled using a Generalized Additive Model (GAM) with a Negative Binomial distribution to account for overdispersion in the response variable. Land cover type (natural and agricultural) was included as ordered factors, while DEM, drainage network density, and lithology classes were included as smooth terms. All smooth terms were fitted using a cubic regression spline basis with shrinkage ("cs") and a basis dimension (k = 4) to balance model complexity and overfitting. Smoothness selection was carried out using restricted maximum likelihood. Model fitting was performed using the mgcv R package [51].

3. Results

3.1. Accuracy of Inundation Mapping

Based on the classification results across different thresholds, the analysis reveals a clear optimal range for flood detection performance, with the F1 score peaking at 0.86 at a threshold of 1.25, indicating the best trade-off between false positives and false negatives. This threshold also produced the highest accuracy (85.91%) with the lowest variability (standard deviation $\approx 0.06 \pm 6.01\%$), demonstrating highly consistent performance across dates. In contrast, lower thresholds (1.05 and 1.15) substantially reduced both F1 scores (0.72 and 0.80, respectively) and accuracy (respectively, 68.58% and 80.10%), reflecting increased misclassification, while higher thresholds (1.35 and 1.45) maintained moderate accuracy (76.70% and 83.01%) but showed declining F1 scores (0.82 and 0.78) and increased

variability (up to 0.15), indicating a more conservative detection bias that missed actual flood events. Collectively, these results establish 1.25 as the most reliable threshold for flooded area classification in this dataset, and it was therefore selected for all subsequent analyses (Figure 3).

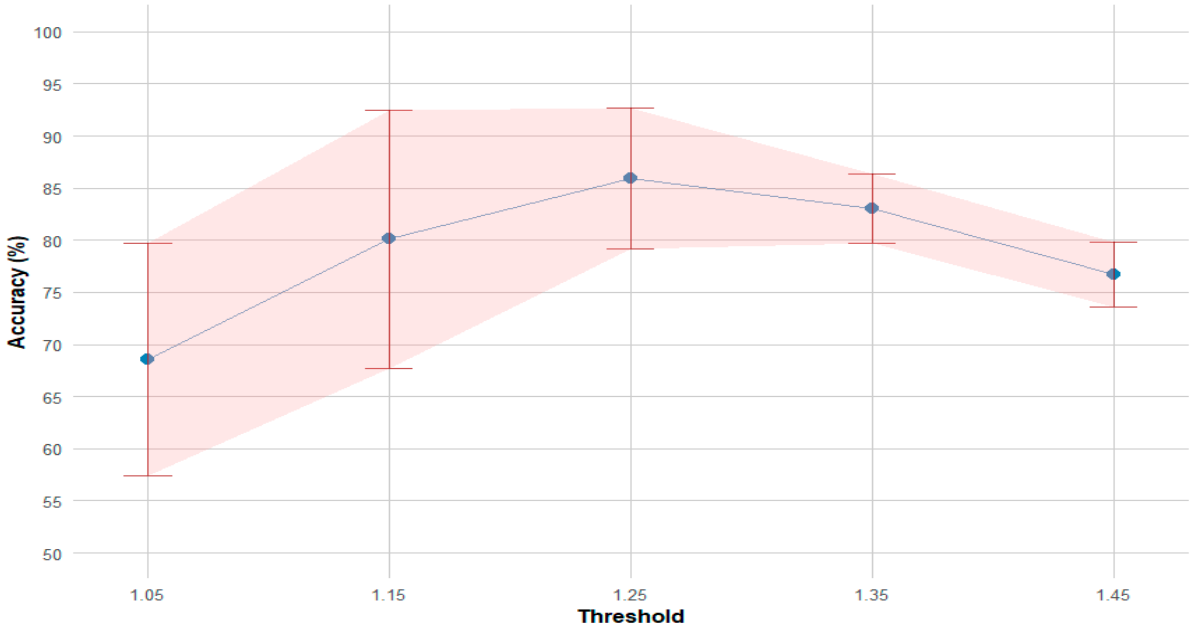

Figure 3. The relationship between the classification threshold value and mean predictive accuracy for flooded area detection. The solid blue line connects the mean accuracy (%) calculated across three different dates. The shaded ribbon and error bars represent the 95% confidence intervals around each mean.

The inundation coverage derived from SAR data, validated using drone imagery, achieved an overall mean accuracy of 85.91% ± 6.01% at the validation sites, with an F1-score of 0.86 ± 0.06, indicating relatively good classification accuracy. However, the classification overestimated inundated areas by 6.47% ± 6.74% and underestimated them by 1.91% ± 7.34% (Table 2).

Table 2. Confusion matrix for the validation of inundation coverage (area) between SAR and drone data.

		SAR	
		True	**False**
Drone	Positive	38.39% ± 14.21%	6.47% ± 6.74%
	Negative	47.52% ± 13.82%	1.91% ± 7.34%

3.2. Inundation Coverage

The inundation mapping analysis of 2015–2019 revealed that the most significant inundation events occur primarily during the winter and spring seasons, beginning in October and extending through April. During this period, the extent of flooding reached its peak, with water covering up to 132 square kilometers, which represents 26% of the entire study area. The most prolonged flood event began in October 2016 and lasted for an extensive seven months, continuing through to the end of April 2017. Remarkably, in the following year, another significant flood event started in October 2017, lasting even longer until the middle of June 2018. These consecutive extended flooding periods emphasize the severity and persistence of water accumulation in the region. Overall, over the five-year

period, flood events remained relatively consistent, interrupted by an exceptional 2017 flood event that extended into 2018, producing unusually severe flooding during both spring snowmelt and autumn rain seasons that year. These two peak flooding events in 2017 stood out as anomalies compared to the otherwise stable pattern observed throughout the rest of the year. Pairwise comparisons using the Wilcoxon rank-sum test indicated that inundated areas in 2017 were significantly higher than in all other years ($p < 0.05$), representing the most pronounced deviation in the dataset. Inundated areas in 2018 also differed significantly from all other years, including 2017. No significant differences were observed among 2015, 2016, and 2019 ($p > 0.05$) (Figure 4).

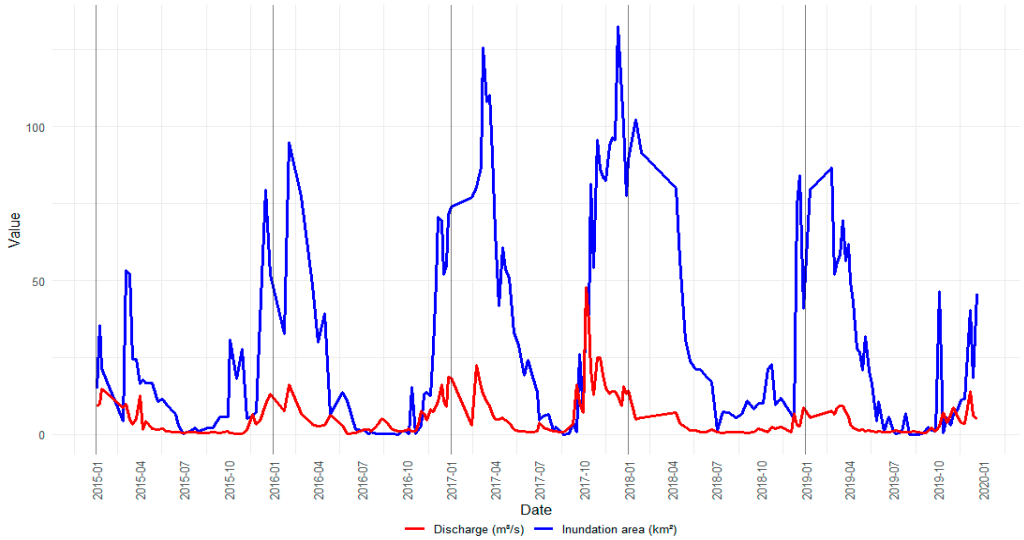

Figure 4. Inundated areas (km^2) and water discharge (m^3/s) within the area of interest based on SAR imagery analysis for the period 2015–2019.

Over a five-year period, certain areas (around Sakūčiai, Žalgiriai, and Leitgiriai forest) experienced inundation for up to 1075 days in total, equivalent to 57% of the time. In contrast, some regions, such as Šturmai village, Šilutė and Pagėgiai cities, and most parts of Beržtai forest, remained water-free throughout the entire five-year span (Figure 5).

3.3. Temporal Relationship Between Water Discharge and Flood Extent

The highest correlation between water discharge and the inundated area occurred 5–10 days after the initial surge in water discharge, with a correlation coefficient of 0.68 in terms of inundation susceptibility. In comparison, when the discharge and inundated area were analyzed without any time delay, the correlation dropped to 0.57. However, cumulative discharge values over 5, 10, and 15 days did not improve prediction accuracy, with results ranging between 0.42 and 0.54 for inundation extent estimation (Table 3).

Table 3. Effect of discharge lag and accumulation on correlation with inundation area.

Type of Data	Correlation Coefficient
no lag	0.57
5 days lag	0.61
10 days lag	0.68
10 days cumulative	0.54
15 days cumulative	0.51

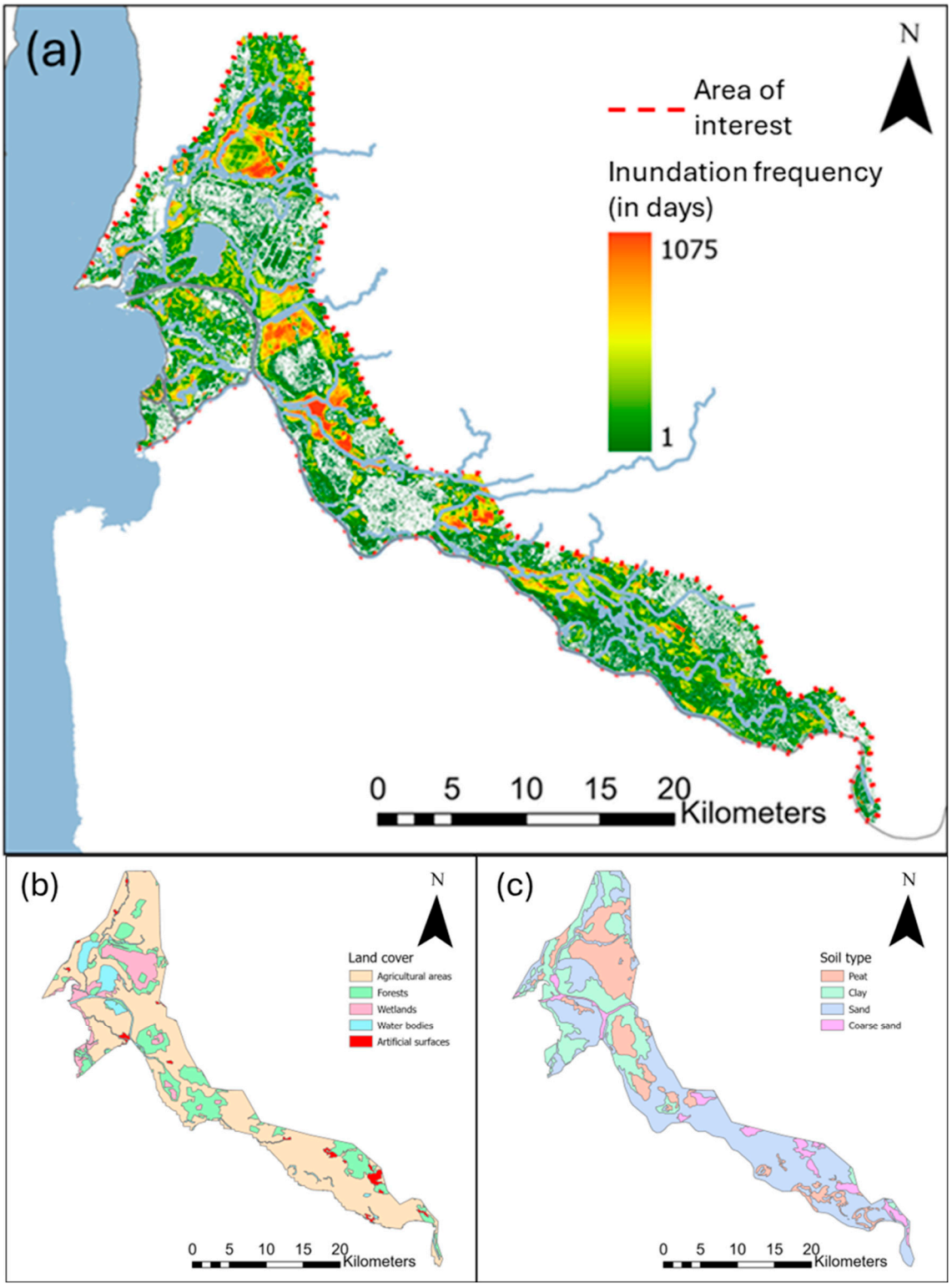

Figure 5. (**a**) Inundation frequency (in days) during a 5-year period (2015–2019), (**b**) land cover types, and (**c**) soil type maps.

3.4. Inundation Dynamics over Land Cover and Lithological Layers

Inundation across different land cover types was most prevalent in agricultural areas, which experienced an average of 113 days of inundation over the five-year period. This accounts for approximately 6.2% of the total time during the study period. In contrast,

natural areas were impacted less frequently by inundation: 23 to 29 days over the five-year period, representing only 1.3% to 1.6% of the time.

Inundation across various lithological layers was most widespread on sapropel surfaces, which lasted an average of 148 days of inundation over a five-year period, making it the most frequently inundated type of surface. In comparison, other lithological layers were less prone to inundation. For example, sand, silt, clay, and peat layers were affected by inundation for an average of 51 to 84 days over the same timeframe. Loam, in contrast, experienced significantly fewer inundation days, with an average of just 27 days of inundation during the five-year period.

The GAM explained 47.6% of the deviance in flood hotspot occurrence. Inundation duration was primarily shaped by topography, with water pooling non-linearly in low-lying areas ($\chi^2 = 17.71$, edf ≈ 2.79, $p < 0.001$). This effect was amplified in fine-grained lithologies ($\chi^2 = 4.46$, edf ≈ 1.10, $p = 0.019$) and further mediated by land cover. The overall influence of land cover was highly significant ($\chi^2 = 71.59$, df = 1, $p < 0.001$), with forests showing markedly reduced inundation frequencies compared to other land types. Beyond this strong main effect, forest cover significantly modified the relationship between flooding and both elevation ($\chi^2 = 58.47$, edf ≈ 2.83, $p < 0.001$) and lithology ($\chi^2 = 1.54$, edf ≈ 0.71, $p = 0.061$). Stream density also exerted an independent non-linear effect ($\chi^2 = 7.23$, edf ≈ 1.64, $p = 0.010$). Together, these results demonstrate that inundation dynamics are jointly governed by elevation, substrate permeability, and land cover, with forests consistently mitigating flood risk even in low-lying, impermeable environments (Figure 6).

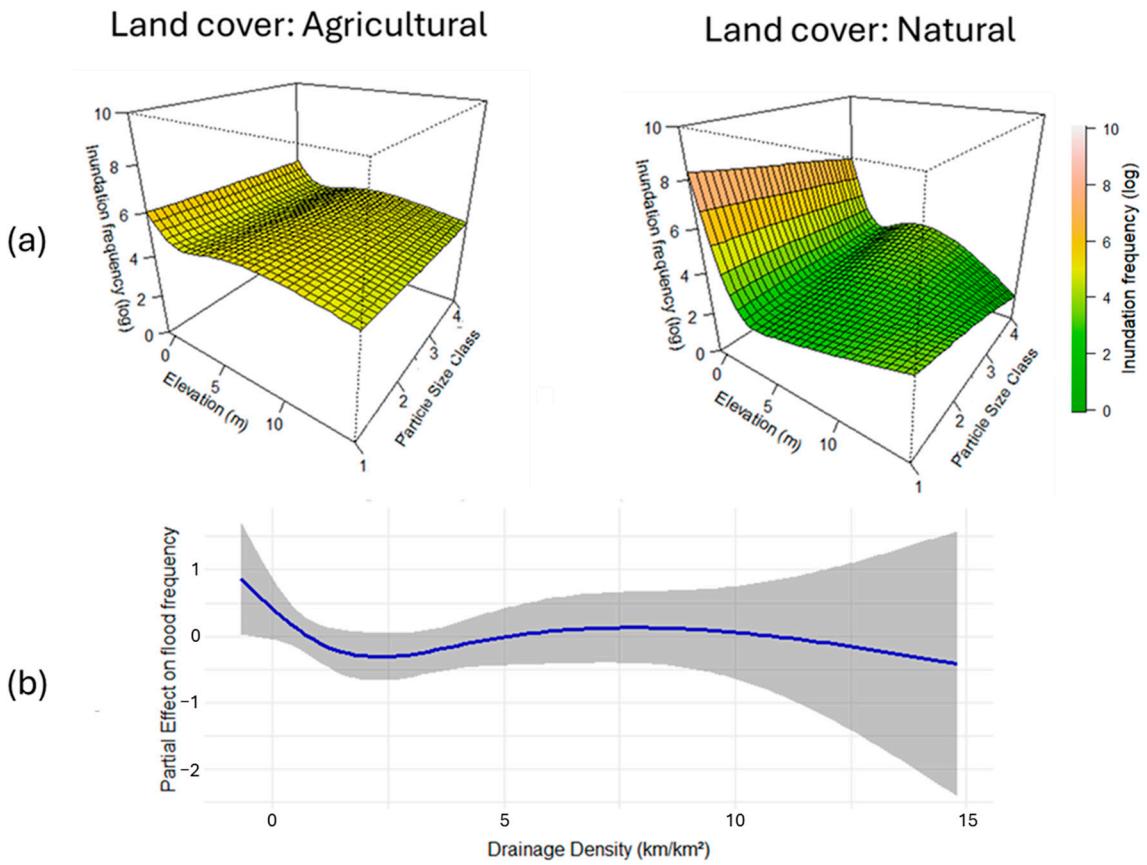

Figure 6. Generalized additive model interaction illustrating (**a**) the relationship between inundated area, DEM, land cover, soil lithological particle size, which is expressed by classes ranging from the finest (1) to the coarsest (4) and (**b**) the relationship between inundated area and drainage network density. The shaded area represents the 95% confidence interval around the estimated smooth.

4. Discussion

The application of the change detection method, combined with drone imagery for validation, demonstrated the potential of SAR and drone imagery for mapping inundated areas in the Nemunas River delta. This study revealed that automating inundation detection can provide valuable insights into the overall status of water-prone areas, enhancing our understanding of yearly seasonal patterns in inundation events.

Drones provided high-resolution imagery that was used to validate inundation patterns derived from SAR data. While drone imagery captured finer details often missed by coarser 10 × 10 square meters SAR imagery, its visual nature posed limitations, particularly in detecting inundation obscured by vegetation. In contrast, SAR's ability to penetrate non-dense vegetation occasionally resulted in overestimation of inundated areas, which was observed in approximately 6.5% of the validation images [52]. SAR allowed us to observe the entire delta in a single acquisition and build a comprehensive time-series analysis of inundation dynamics over the 2015–2019 period. Ultimately, although drone-based validation may not be as precise as in situ measurements, it remains a critical complementary method, offering high-resolution insights and accessibility that significantly contribute to the accuracy of inundation assessments.

Despite the promising validation results, several limitations should be considered. First, snow cover during colder months may interfere with SAR backscatter signals, potentially leading to misclassification of inundated areas. Second, the use of outdated land cover datasets may not accurately reflect recent changes such as urban development or agricultural expansion, which can affect inundation dynamics. Third, drone imagery, while high-resolution, is limited by its visual nature and may fail to detect water obscured by dense vegetation. Additionally, the threshold value used for inundation classification (1.25× VH backscatter) may not be universally applicable across different regions or flood types, and its effectiveness could vary under different environmental conditions. These limitations highlight the need for cautious interpretation and underscore the importance of integrating multiple data sources for robust flood mapping.

The selection of an optimal threshold is a critical and often site-specific step in SAR-based flood mapping [10,44,53]. To provide a detailed elaboration of the underlying mechanisms and their response to land cover, we analyzed performance across a range of thresholds within the natural and agricultural land. This analysis reveals a clear relationship between the threshold value in our deltaic environment, which is dominated by open water and vegetated areas (primarily agriculture). The optimal threshold of 1.25 was determined, which effectively balances between false positives (at <1.25 misclassifying moist soil or calm open water as flooded) and false negatives (at >1.25 missing flooded vegetation where the double-bounce effect generates high backscatter).

Much of the Nemunas Delta within the area of interest experienced inundation, primarily because it lacks protection from levees. During the research period (2015–2019), two extreme flooding events occurred in 2017, inundating vast delta areas. In contrast, the other years exhibited typical seasonal flooding patterns. However, flooding in the delta is regulated by the operation of pumping stations near Rusnė Island. These stations maintain dryness in certain low-lying areas of the floodplain, even though they are situated at a lower elevation than the surrounding fields [40]. This impact complicates inundation mapping efforts when modeling only Digital Elevation Models (DEMs) with water discharge data from water level measuring stations, as elevation data does not fully capture these water management interventions. Consequently, satellite imagery has proven to be one of the most dependable tools for continuously tracking inundation patterns across the extensive Nemunas Delta. By integrating both DEM and SAR imagery, we successfully classified inundated areas affected by human-made hydrostructures that could complicate

detection using DEM alone. Additionally, we successfully classified inundated areas in dense vegetation by utilizing DEM to fill in gaps where SAR data could not penetrate.

The observed 5 to 10-day delay between the initial rise in water discharge and the subsequent expansion of inundation is consistent with findings from similar studies conducted in the Nemunas Delta region [54]. This pattern and continuous monitoring of water discharge can enhance the prediction of the overall extent of inundation and the specific areas impacted. This is especially relevant during Sentinel-1 imagery acquisition gaps (up to 5 days), which might be too long to enable timely action during a flooding event. By using early water discharge data to forecast flood progression, governmental agencies can enhance their readiness and mitigate potential impacts on affected communities.

These findings highlight the seasonal nature of inundation in the region, with the greatest inundation occurring during the colder months and the early spring thaw. Flooding events during the summer months, which were exclusively caused by heavy rainfall, with the resulting floods typically lasting for a duration of up to two weeks [40,54].

The variation in the inundation occurrence was mainly explained by the interaction effect of lithology and land cover. It was expected that the inundation occurrence linearly increased with the decrease in soil grain size in agricultural areas, while this trend was not clear in forested areas, as forest vegetation may buffer lithologically driven flood patterns, maintaining hydrological stability [55]. Agricultural lands were significantly more prone to prolonged inundation events compared to natural land types due to deteriorated soil, which affects water absorption rates. The topography of such areas is usually flat, resulting in widespread distribution in water-prone zones. The conversion of natural vegetation to agricultural land, along with land modifications such as soil compaction from heavy machinery, irrigation systems, artificial drainage, and animal treading, significantly reduces the soil's capacity to absorb and drain excess water [56,57]. Consequently, inundated agricultural areas may cause significant economic impacts, including crop loss, soil degradation, increased carbon dioxide and methane emissions, and delays in planting or harvesting cycles [58–61]. Furthermore, the most inundated layers commonly are composed of sand, silt, and peat, as well as agricultural and fine-grained lithological layers. Their fine texture and low permeability slow water infiltration, causing these layers to retain water for prolonged periods [62]. The drainage network density emerged as an important hydrological control. Higher drainage densities were associated with increased flood peaks and discharge volumes, but paradoxically, they also contributed to reduced inundation extent and depth due to faster water conveyance and shorter concentration times [63,64]. This dual role highlights the importance of considering both network topology and land cover interactions when assessing flood risk.

The Environmental Protection Agency provides flood risk maps developed for the Nemunas Delta as well as for all of Lithuania, and these maps are readily accessible online [65]. The creation of these maps involved the use of orthophotogrammetry, digital elevation models, and ground-based data collected through global navigation satellite system technology [66]. These maps serve as a valuable resource for understanding and managing flood risks across the region. However, due to the unpredictable nature of floodwaters and the challenging accessibility of some affected areas, this traditional approach requires significantly more time to collect all data, and flood extent can only be predicted. In contrast, satellite imagery offers a more efficient and comprehensive solution. Since the launch of the Sentinel-1 mission in 2015, it has been possible to continuously monitor inundation dynamics in the Nemunas Delta over a chosen time period. This method provides near-real-time updates, ensuring better risk awareness and reducing the reliance on labor-intensive ground surveys.

In this study, we implemented a method that utilizes both drone and Synthetic Aperture Radar (SAR) imagery for inundation monitoring over a five-year period. The approach has proven effective, and its potential can be further extended, as the inundation classification process is automated. This work process can be used in many water-prone areas that are not heavily forested, making it useful for analyzing and tracking inundation patterns over long durations. The scalability and automation of the system ensure that it can be used to monitor inundation dynamics over extended time periods in diverse geographical regions.

Building on the findings of this study, future research could explore several avenues to enhance inundation mapping. Incorporating Sentinel-2 and MODIS multispectral data could improve land cover classification and help distinguish between water and other low-reflectance surfaces. The use of machine learning techniques, such as Random Forest or Convolutional Neural Networks, could further refine classification accuracy by capturing complex patterns in SAR and optical data. Developing automated, real-time flood monitoring systems that combine SAR, drone, and hydrological data would support early warning efforts and disaster response. Moreover, in situ data collection could provide valuable ground truth for calibration and validation, especially in areas with complex hydrological behavior. Finally, long-term monitoring using remote sensing could contribute to climate change impact assessments, helping to understand shifts in flood frequency, intensity, and spatial distribution in the Nemunas Delta and similar deltaic regions.

5. Conclusions

The high inundation mapping accuracy (86% against drone data), achieved through an optimized change detection threshold that maximized the F1-score (0.86), provides strong confidence in the data derived from the Sentinel-1. The maximum inundation was determined during spring snowmelt and colder months, with shorter, rainfall-driven summer floods. Approximately 60% of inundated areas were low-lying agricultural fields.

Inundation duration is primarily driven by topography, with water pooling non-linearly in lower elevations. This effect is intensified by fine-grained lithology (e.g., silt, peat) and mediated by land cover, as forests are associated with shorter inundation than agricultural lands. This demonstrates the capacity of forests to mitigate flooding even in low-lying areas with impermeable soils.

The 10-day lag between the initial increase in water discharge and the peak inundation extent was revealed. The prolonged delay can likely be attributed to the flat and expansive nature of the delta, which causes water to disperse gradually over an extended time period.

Author Contributions: J.G.: conceptualization, methodology, software, validation, formal analysis, investigation, resources, data curation, writing—original draft, writing—review and editing, visualization, supervision; M.B.: conceptualization, methodology, validation, investigation, resources, data curation, writing—review and editing, supervision; D.V.: conceptualization, resources, data curation, writing—review and editing, supervision; E.T.: conceptualization, methodology, validation, investigation, resources, writing—review and editing. All authors have read and agreed to the published version of the manuscript.

Funding: This research was supported by a doctoral scholarship program in Physical Geography at Klaipeda University, Lithuania, and was partly supported by RESTORE4Cs project funded by the European Union's Horizon Europe research and innovation programme (grant agreement 101056782).

Data Availability Statement: The data presented in this study are available on request from the corresponding author.

Conflicts of Interest: The authors declare no conflicts of interest.

References

1. Edmonds, D.A.; Caldwell, R.L.; Brondizio, E.S.; Siani, S.M. Coastal Flooding Will Disproportionately Impact People on River Deltas. *Nat. Commun.* **2020**, *11*, 4741. [CrossRef]
2. Madsen, H.; Lawrence, D.; Lang, M.; Martinkova, M.; Kjeldsen, T.R. Review of Trend Analysis and Climate Change Projections of Extreme Precipitation and Floods in Europe. *J. Hydrol.* **2014**, *519*, 3634–3650. [CrossRef]
3. Tradowsky, J.S.; Philip, S.Y.; Kreienkamp, F.; Kew, S.F.; Lorenz, P.; Arrighi, J.; Bettmann, T.; Caluwaerts, S.; Chan, S.C.; De Cruz, L.; et al. Attribution of the Heavy Rainfall Events Leading to Severe Flooding in Western Europe during July 2021. *Clim. Change* **2023**, *176*, 90. [CrossRef]
4. Anghileri, D.; Pianosi, F.; Soncini-Sessa, R. Trend Detection in Seasonal Data: From Hydrology to Water Resources. *J. Hydrol.* **2014**, *511*, 171–179. [CrossRef]
5. Coopersmith, E.J.; Minsker, B.S.; Sivapalan, M. Patterns of Regional Hydroclimatic Shifts: An Analysis of Changing Hydrologic Regimes. *Water Resour. Res.* **2014**, *50*, 1960–1983. [CrossRef]
6. Fowler, K.; Peel, M.; Saft, M.; Nathan, R.; Horne, A.; Wilby, R.; McCutcheon, C.; Peterson, T. Hydrological Shifts Threaten Water Resources. *Water Resour. Res.* **2022**, *58*, e2021WR031210. [CrossRef]
7. Strohmenger, L.; Ackerer, P.; Belfort, B.; Pierret, M.C. Local and Seasonal Climate Change and Its Influence on the Hydrological Cycle in a Mountainous Forested Catchment. *J. Hydrol.* **2022**, *610*, 127914. [CrossRef]
8. Caballero, I.; Ruiz, J.; Navarro, G. Sentinel-2 Satellites Provide near-Real Time Evaluation of Catastrophic Floods in the West Mediterranean. *Water* **2019**, *11*, 2499. [CrossRef]
9. Goffi, A.; Stroppiana, D.; Brivio, P.A.; Bordogna, G.; Boschetti, M. Towards an Automated Approach to Map Flooded Areas from Sentinel-2 MSI Data and Soft Integration of Water Spectral Features. *Int. J. Appl. Earth Obs. Geoinf.* **2020**, *84*, 101951. [CrossRef]
10. Huang, M.; Jin, S. Rapid Flood Mapping and Evaluation with a Supervised Classifier and Change Detection in Shouguang Using Sentinel-1 SAR and Sentinel-2 Optical Data. *Remote Sens.* **2020**, *12*, 2073. [CrossRef]
11. Konapala, G.; Kumar, S.V.; Ahmad, S.K. Exploring Sentinel-1 and Sentinel-2 Diversity for Flood Inundation Mapping Using Deep Learning. *ISPRS J. Photogramm. Remote Sens.* **2021**, *180*, 163–173. [CrossRef]
12. Post, P.; Aun, M. Changes in Satellite-Based Cloud Parameters in the Baltic Sea Region during Spring and Summer (1982–2015). *Adv. Sci. Res.* **2020**, *17*, 219–225. [CrossRef]
13. Tarpanelli, A.; Mondini, A.C.; Camici, S. Effectiveness of Sentinel-1 and Sentinel-2 for Flood Detection Assessment in Europe. *Nat. Hazards Earth Syst. Sci.* **2022**, *22*, 2473–2489. [CrossRef]
14. Amitrano, D.; Di Martino, G.; Iodice, A.; Riccio, D.; Ruello, G. Unsupervised Rapid Flood Mapping Using Sentinel-1 GRD SAR Images. *IEEE Trans. Geosci. Remote Sens.* **2018**, *56*, 3290–3299. [CrossRef]
15. Amitrano, D.; Di Martino, G.; Di Simone, A.; Imperatore, P. Flood Detection with SAR: A Review of Techniques and Datasets. *Remote Sens.* **2024**, *16*, 656. [CrossRef]
16. Pelich, R.; Chini, M.; Hostache, R.; Matgen, P.; Delgado, J.M.; Sabatino, G. Towards a Global Flood Frequency Map from SAR Data. In Proceedings of the 2017 IEEE International Geoscience and Remote Sensing Symposium (IGARSS), Fort Worth, TX, USA, 23–28 July 2017; IEEE: Fort Worth, TX, USA, 2017; pp. 4024–4027.
17. Li, R.; Liu, W.; Yang, L.; Sun, S.; Hu, W.; Zhang, F.; Li, W. DeepUNet: A Deep Fully Convolutional Network for Pixel-Level Sea-Land Segmentation. *IEEE J. Sel. Top. Appl. Earth Obs. Remote Sens.* **2018**, *11*, 3954–3962. [CrossRef]
18. Long, S.; Fatoyinbo, T.E.; Policelli, F. Flood Extent Mapping for Namibia Using Change Detection and Thresholding with SAR. *Environ. Res. Lett.* **2014**, *9*, 035002. [CrossRef]
19. Landuyt, L.; Van Coillie, F.M.; Vogels, B.; Dewelde, J.; Verhoest, N.E. Towards Operational Flood Monitoring in Flanders Using Sentinel-1. *IEEE J. Sel. Top. Appl. Earth Obs. Remote Sens.* **2021**, *14*, 11004–11018. [CrossRef]
20. Liang, J.; Liu, D. A Local Thresholding Approach to Flood Water Delineation Using Sentinel-1 SAR Imagery. *ISPRS J. Photogramm. Remote Sens.* **2020**, *159*, 53–62. [CrossRef]
21. Uddin, K.; Matin, M.A.; Meyer, F.J. Operational Flood Mapping Using Multi-Temporal Sentinel-1 SAR Images: A Case Study from Bangladesh. *Remote Sens.* **2019**, *11*, 1581. [CrossRef]
22. Tsyganskaya, V.; Martinis, S.; Marzahn, P.; Ludwig, R. SAR-Based Detection of Flooded Vegetation—A Review of Characteristics and Approaches. *Int. J. Remote Sens.* **2018**, *39*, 2255–2293. [CrossRef]
23. Misra, A.; White, K.; Nsutezo, S.F.; Straka III, W.; Lavista, J. Mapping Global Floods with 10 Years of Satellite Radar Data. *Nat. Commun.* **2025**, *16*, 5762. [CrossRef]
24. Alonso-Sarria, F.; Valdivieso-Ros, C.; Molina-Pérez, G. Detecting Flooded Areas Using Sentinel-1 SAR Imagery. *Remote Sens.* **2025**, *17*, 1368. [CrossRef]
25. Manakos, I.; Kordelas, G.A.; Marini, K. Fusion of Sentinel-1 Data with Sentinel-2 Products to Overcome Non-Favourable Atmospheric Conditions for the Delineation of Inundation Maps. *Eur. J. Remote Sens.* **2020**, *53*, 53–66. [CrossRef]
26. Martinis, S.; Plank, S.; Ćwik, K. The Use of Sentinel-1 Time-Series Data to Improve Flood Monitoring in Arid Areas. *Remote Sens.* **2018**, *10*, 583. [CrossRef]

27. Tran, K.H.; Menenti, M.; Jia, L. Surface Water Mapping and Flood Monitoring in the Mekong Delta Using Sentinel-1 SAR Time Series and Otsu Threshold. *Remote Sens.* **2022**, *14*, 5721. [CrossRef]
28. Greifeneder, F.; Wagner, W.; Sabel, D.; Naeimi, V. Suitability of SAR Imagery for Automatic Flood Mapping in the Lower Mekong Basin. In *Remote Sensing the Mekong*; Routledge: Oxfordshire, UK, 2018; pp. 111–128.
29. Hong Quang, N.; Tuan, V.A.; Thi Thu Hang, L.; Manh Hung, N.; Thi The, D.; Thi Dieu, D.; Duc Anh, N.; Hackney, C.R. Hydrological/Hydraulic Modeling-Based Thresholding of Multi SAR Remote Sensing Data for Flood Monitoring in Regions of the Vietnamese Lower Mekong River Basin. *Water* **2019**, *12*, 71. [CrossRef]
30. Pandey, A.C.; Kaushik, K.; Parida, B.R. Google Earth Engine for Large-Scale Flood Mapping Using SAR Data and Impact Assessment on Agriculture and Population of Ganga-Brahmaputra Basin. *Sustainability* **2022**, *14*, 4210. [CrossRef]
31. Kjerfve, B. Coastal Lagoons. In *Elsevier Oceanography Series*; Elsevier: Amsterdam, The Netherlands, 1994; Volume 60, pp. 1–8.
32. Lang, F.; Zhu, Y.; Zhao, J.; Hu, X.; Shi, H.; Zheng, N.; Zha, J. Flood Mapping of Synthetic Aperture Radar (SAR) Imagery Based on Semi-Automatic Thresholding and Change Detection. *Remote Sens.* **2024**, *16*, 2763. [CrossRef]
33. Li, Y.; Martinis, S.; Wieland, M.; Schlaffer, S.; Natsuaki, R. Urban Flood Mapping Using SAR Intensity and Interferometric Coherence via Bayesian Network Fusion. *Remote Sens.* **2019**, *11*, 2231. [CrossRef]
34. Žaromskis, R. *Nemuno Delta: Monografija*; Klaipėdos Universiteto Leidykla: Klaipeda, Lithuania, 2013.
35. Dubra, V.; Abromas, J.; Dumbrauskas, A. Impact of Ice Regime in the Nemunas River and the Curonian Lagoon on Floods in the Delta Area. *Rural Dev. Proc.* **2013**, *6*, 239–244.
36. Stonevičius, E.; Rimkus, E.; Štaras, A.; Kažys, J.; Valiuškevičius, G. Climate Change Impact on the Nemunas River Basin Hydrology in the 21st Century. *Boreal Environ. Res.* **2017**, *22*, 49.
37. Čerkasova, N.; Mėžinė, J.; Idzelytė, R.; Lesutienė, J.; Ertürk, A.; Umgiesser, G. Exploring Variability in Climate Change Projections on the Nemunas River and Curonian Lagoon: Coupled SWAT and SHYFEM Modeling Approach. *Ocean Sci.* **2024**, *20*, 1123–1147. [CrossRef]
38. Čerkasova, N.; Mėžinė, J.; Idzelytė, R.; Lesutienė, J.; Erturk, A.; Umgiesser, G. Modeling Climate Change Uncertainty and Its Impact on the Nemunas River Watershed and Curonian Lagoon Ecosystem. *EGUsphere* **2024**, *2024*, 1–28. [CrossRef]
39. Idzelytė, R.; Čerkasova, N.; Mėžinė, J.; Dabulevičienė, T.; Razinkovas-Baziukas, A.; Ertürk, A.; Umgiesser, G. Coupled Hydrological and Hydrodynamic Modelling Application for Climate Change Impact Assessment in the Nemunas River Watershed–Curonian Lagoon–Southeastern Baltic Sea Continuum. *Ocean Sci.* **2023**, *19*, 1047–1066. [CrossRef]
40. Dumbrauskas, A.; Punys, P. Character of Floods of the Nemunas River Delta. In Proceedings of the International Conference Towards Natural Flood Reduction Strategies, Warsaw, Poland, 6–13 September 2003; pp. 1–7.
41. Grimaldi, S.; Xu, J.; Li, Y.; Pauwels, V.R.; Walker, J.P. Flood Mapping under Vegetation Using Single SAR Acquisitions. *Remote Sens. Environ.* **2020**, *237*, 111582. [CrossRef]
42. Iqbal, U.; Riaz, M.Z.B.; Zhao, J.; Barthelemy, J.; Perez, P. Drones for Flood Monitoring, Mapping and Detection: A Bibliometric Review. *Drones* **2023**, *7*, 32. [CrossRef]
43. Gorelick, N.; Hancher, M.; Dixon, M.; Ilyushchenko, S.; Thau, D.; Moore, R. Google Earth Engine: Planetary-Scale Geospatial Analysis for Everyone. *Remote Sens. Environ.* **2017**, *202*, 18–27. [CrossRef]
44. UN-SPIDER Step-by-Step: Recommended Practice: Flood Mapping and Damage Assessment Using Sentinel-1 SAR Data in Google Earth Engine | UN-SPIDER Knowledge Portal. Available online: https://www.un-spider.org/advisory-support/recommended-practices/recommended-practice-google-earth-engine-flood-mapping/step-by-step (accessed on 18 February 2022).
45. ESRI Environmental Systems Research Institute (ESRI). *ArcGIS Pro Release 3.0.1.*; ESRI: Redlands, CA, USA, 2022.
46. Lietuvos Geologijos Tarnyba Lietuvos Geologijos Tarnybos El. Paslaugos. Available online: https://www.lgt.lt/epaslaugos/index.xhtml (accessed on 16 June 2025).
47. European Environment Agency (EEA) Corine Land Cover 2018. Available online: https://land.copernicus.eu/en/products/corine-land-cover/clc2018 (accessed on 4 June 2025).
48. Benesty, J.; Chen, J.; Huang, Y.; Cohen, I. Pearson Correlation Coefficient. In *Noise Reduction in Speech Processing*; Springer Topics in Signal Processing; Springer: Berlin/Heidelberg, Germany, 2009; Volume 2, pp. 1–4, ISBN 978-3-642-00295-3.
49. Haynes, W. Wilcoxon Rank Sum Test. In *Encyclopedia of Systems Biology*; Springer: New York, NY, USA, 2013; pp. 2354–2355, ISBN 978-1-4419-9863-7.
50. R Core Team. *R: A Language and Environment for Statistical Computing*; R Core Team: Vienna, Austria, 2025.
51. Wood, S.N. Fast Stable Restricted Maximum Likelihood and Marginal Likelihood Estimation of Semiparametric Generalized Linear Models. *J. R. Stat. Soc. Ser. B Stat. Methodol.* **2011**, *73*, 3–36.
52. Marchetti, G.; Manconi, A.; Comiti, F. Limitations in the Use of Sentinel-1 Data for Morphological Change Detection in Rivers. *Int. J. Remote Sens.* **2023**, *44*, 6642–6669. [CrossRef]
53. Pulvirenti, L.; Chini, M.; Pierdicca, N.; Guerriero, L.; Ferrazzoli, P. Flood Monitoring Using Multi-Temporal COSMO-SkyMed Data: Image Segmentation and Signature Interpretation. *Remote Sens. Environ.* **2011**, *115*, 990–1002. [CrossRef]

54. Valiuskevičius, G.; Stonevičius, E.; Stankunavičius, G.; Brastovickyté-Stankevič, J. Severe Floods in Nemunas River Delta. *Baltica* **2018**, *31*, 89. [CrossRef]
55. Osman, K.T. Physical Properties of Forest Soils. In *Forest Soils*; Springer International Publishing: Cham, Switzerland, 2013; pp. 19–44, ISBN 978-3-319-02540-7.
56. De Jonge, L.W.; Jacobsen, O.H.; Moldrup, P. Soil Water Repellency: Effects of Water Content, Temperature, and Particle Size. *Soil Sci. Soc. Am. J.* **1999**, *63*, 437–442. [CrossRef]
57. Tian, Y.Q.; McDowell, R.; Yu, Q.; Sheath, G.W.; Carlson, W.T.; Gong, P. Modelling to Analyse the Impacts of Animal Treading Effects on Soil Infiltration. *Hydrol. Process.* **2007**, *21*, 1106–1114. [CrossRef]
58. Blackburn, S.R.; Stanley, E.H. Floods Increase Carbon Dioxide and Methane Fluxes in Agricultural Streams. *Freshw. Biol.* **2021**, *66*, 62–77. [CrossRef]
59. Kapović Solomun, M.; Ferreira, C.S.S.; Zupanc, V.; Ristić, R.; Drobnjak, A.; Kalantari, Z. Flood Legislation and Land Policy Framework of EU and non-EU Countries in Southern Europe. *WIREs Water* **2022**, *9*, e1566. [CrossRef]
60. Kundzewicz, Z.W.; Pińskwar, I.; Brakenridge, G.R. Changes in River Flood Hazard in Europe: A Review. *Hydrol. Res.* **2017**, *49*, 294–302. [CrossRef]
61. Paprotny, D.; Sebastian, A.; Morales-Nápoles, O.; Jonkman, S.N. Trends in Flood Losses in Europe over the Past 150 Years. *Nat. Commun.* **2018**, *9*, 1985. [CrossRef]
62. Sofia, G.; Nikolopoulos, E.I. Floods and Rivers: A Circular Causality Perspective. *Sci. Rep.* **2020**, *10*, 5175. [CrossRef]
63. Wu, P.; Wang, T.; Wang, Z.; Song, C.; Chen, X. Impact of Drainage Network Structure on Urban Inundation Within a Coupled Hydrodynamic Model. *Water* **2025**, *17*, 990. [CrossRef]
64. Pallard, B.; Castellarin, A.; Montanari, A. A Look at the Links between Drainage Density and Flood Statistics. *Hydrol. Earth Syst. Sci.* **2009**, *13*, 1019–1029. [CrossRef]
65. Aplinkos Apsaugos Agentūra Potvynių Grėsmės Ir Rizikos Žemėlapis. Available online: https://experience.arcgis.com/experience/7f2d4ca0c74c4857a0620967e530fa4d (accessed on 16 June 2025).
66. Aplinkos Apsaugos Agentūra Potvynių Grėsmės Ir Rizikos Žemėlapių Duomenų Atnaujinimo Paslaugų Ataskaita. Available online: https://aaa.lrv.lt/uploads/aaa/documents/files/Metodika_20220509.pdf (accessed on 15 November 2024).